nature electronics

Article https://doi.org/10.1038/s41928-022-00841-8

An interactive mouthguard based on mechanoluminescence-powered optical fibre sensors for bite-controlled device operation

In the format provided by the authors and unedited

Supplementary Information

Mechanoluminescence-Assisted Interactive Mouthguard for Bite-Controlled Device Operation

Bo Hou[1,†], Luying Yi[1,†], Chao Li[2,3], He Zhao[1], Rong Zhang[2], Bin Zhou[2*] & Xiaogang Liu[1,4,5*]

[1]Department of Chemistry, National University of Singapore, Singapore 117543, Singapore.
[2]Department of Precision Instruments, Tsinghua University, Beijing 100084, China.
[3]Department of Spaceborne Microwave Remote Sensing System, Aerospace Information Research Institute, Chinese Academy of Sciences, Beijing 100190, China.
[4]Joint School of National University of Singapore and Tianjin University, International Campus of Tianjin University, Binhai New City, Fuzhou 350207, China.
[5]Center for Functional Materials, National University of Singapore Suzhou Research Institute, Suzhou 215123, China.

*Corresponding author. E-mail: chmlx@nus.edu.sg (X.L.); zhoub@mail.tsinghua.edu.cn (B.Z.)
†These authors contributed equally to this work.

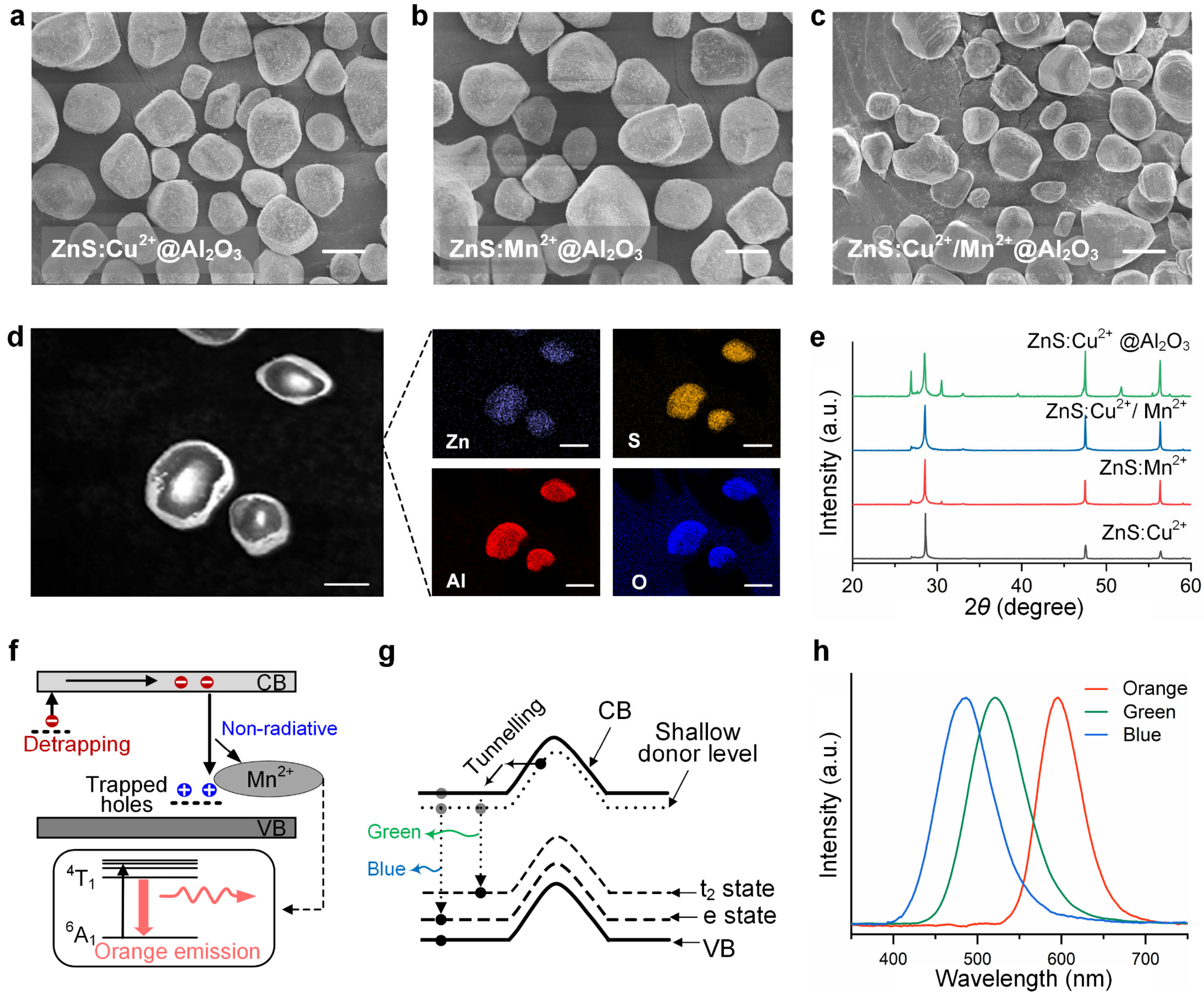

Extended Data Fig. 1 | Characterization of mechanoluminescent phosphors. a–c, Scanning electron microscopy images of Al_2O_3-coated ZnS:M (M = Cu^{2+} or Mn^{2+}) microparticles (10–30 μm). **d**, Energy dispersive X-ray spectroscopy of ZnS@Al_2O_3 samples. **e**, Powder X-ray diffraction patterns of ZnS:M microparticles. Scale bars for **a**–**d** are 20 μm. **f**, Mechanoluminescence mechanism of ZnS:Mn phosphors. The material under stress releases trapped electrons into the conduction band (CB). Instead of emitting radiation, electrons recombine with hole centers or transfer to the valence band (VB), releasing energy release that activates Mn^{2+} ions. The excited Mn^{2+} ion returns to the ground state and emits orange light. **g**, Mechanoluminescence mechanism of ZnS:Cu phosphors. Plastic deformation leads to band bending, and tapped electrons migrate to the conduction band through tunneling. When these electrons recombine with the holes trapped in the t_2 or e state of Cu, green and blue light are emitted. **h**, Mechanoluminescence spectra of phosphors: orange emission (595 nm, ZnS:Cu^{2+}/Mn^{2+}@Al_2O_3), green and blue emission (525 nm and 475 nm, ZnS:Cu^{2+}/Cu^{+}@Al_2O_3).

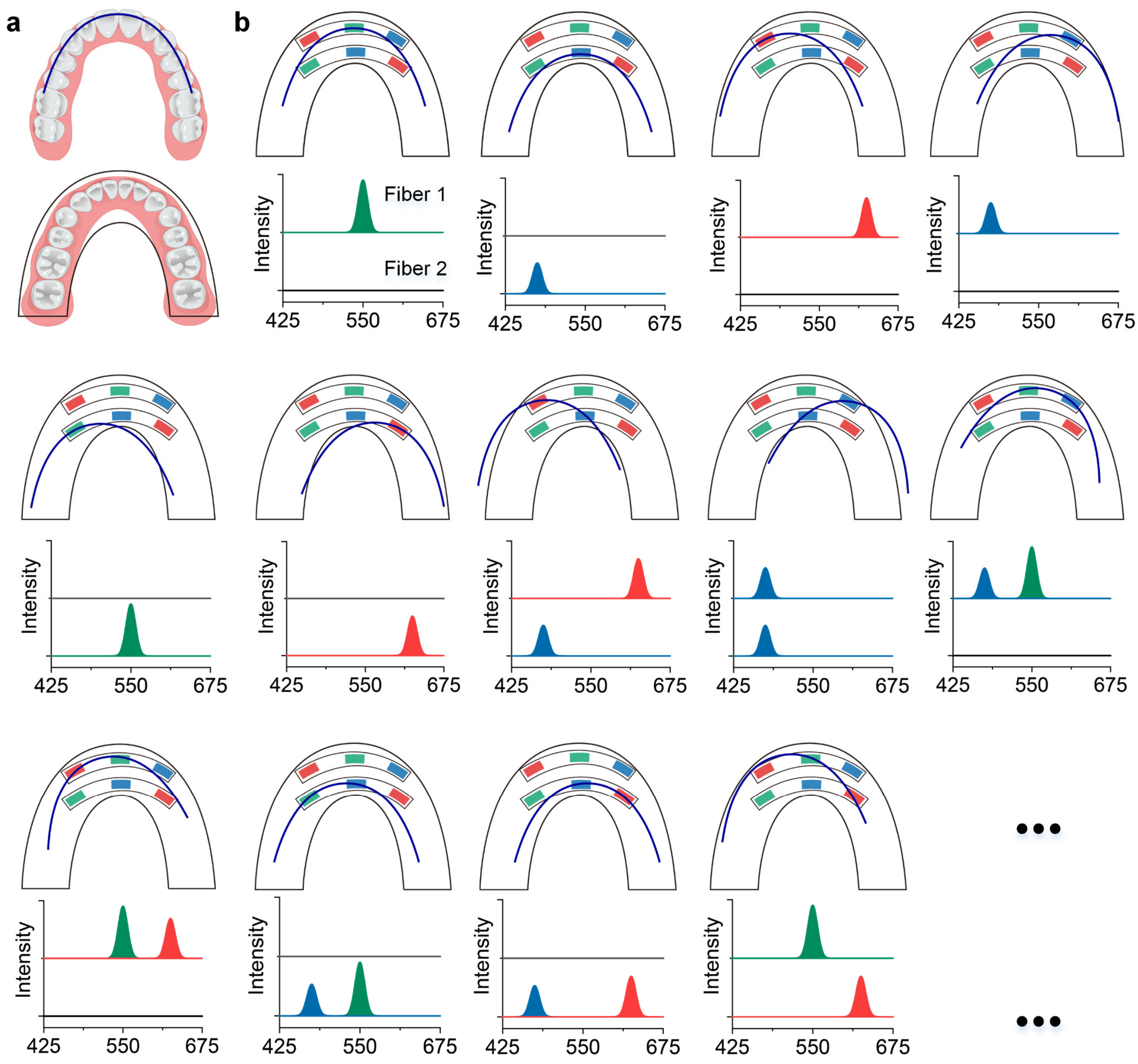

Extended Data Fig. 2 | Dynamic pattern analysis of occlusal contacts using mechanoluminescent pads. a, Schematic of upper and lower tooth contours of an adult with normal occlusion. **b,** Different occlusal patterns (top) and corresponding spectra (bottom). Permutation and combination theory predicts 21 combinations when biting one or two luminescent pads ($C_6^1 + C_6^2 = 21$). The upper tooth contour in **a** (blue line) and the mouthguard contour in **b** (black line) are identifical to ensure that bite patterns are feasible.

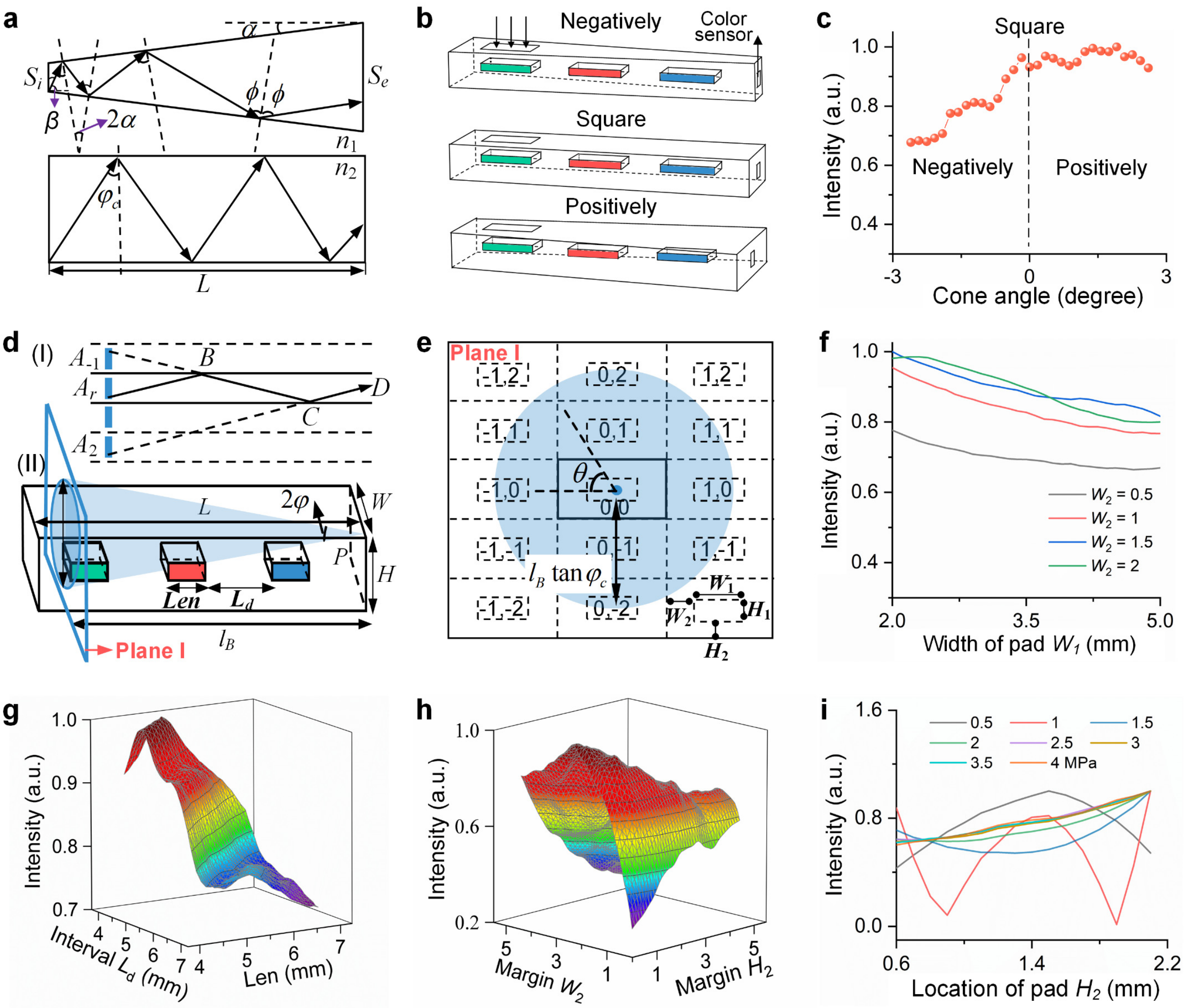

Extended Data Fig. 3 | Optical fiber designs with different geometries. a, Two-dimensional schematic representation of a tapered fiber (top, $S_i \neq S_e$) and a square fiber (bottom, $S_i = S_e$), where α is the cone angle, ϕ is the incident angle of each reflection, β is the collection angle, and φ_c is the critical angle. **b,** Three-dimensional structures of a positively tapered fiber (top, $S_i < S_e$), square fiber (middle), and negatively tapered fiber (bottom, $S_i > S_e$). **c,** Output light intensity versus cone angle. The transmittance of the luminescent pads is 5%. **d,** Equivalent model for imaging. In (I), the reflected ray BC is originally emitted from point A_r of the real light source, and ray BC is equivalent to the virtual ray $A_{-1}C$. Points A_{-1} and A_r are symmetrical about the top plane of the optical fiber. Multiple reflections generate multiple virtual sources. (II) presents the mapping of angular coordinates onto the virtual source plane (plane Ⅰ) in **e**. **e,** Virtual source plane, with each source labeled by its indices (i, j) (e.g., the real source is (**0, 0**)). The power of point P is actually the integral of the power density of the light source in the blue circle with a radius of $l_B \tan(\varphi_c)$ centered on point P. ***Len***, ***W_1***, and ***H_1*** are the length, width, and thickness of luminescent pads, respectively. ***L_d*** is the interval between pads. The total width of the optical fiber is ***W*** $= W_1 + 2W_2$, and the total thickness of the fiber is ***H*** $= H_1 + 2H_2$. ***W_2*** and ***H_2*** are the difference in center coordinate between the luminescent pad and waveguide in lateral and horizontal projections, respectively. **f,** Intensity versus width W_1 under different W_2. **g,** Intensity under different L_d and Len. **h,** Intensity under different W_2 and H_2. **i,** Intensity versus location H_2. The luminescent pad's Young's modulus is 1 MPa, while the optical fiber's is 0.5–4 MPa.

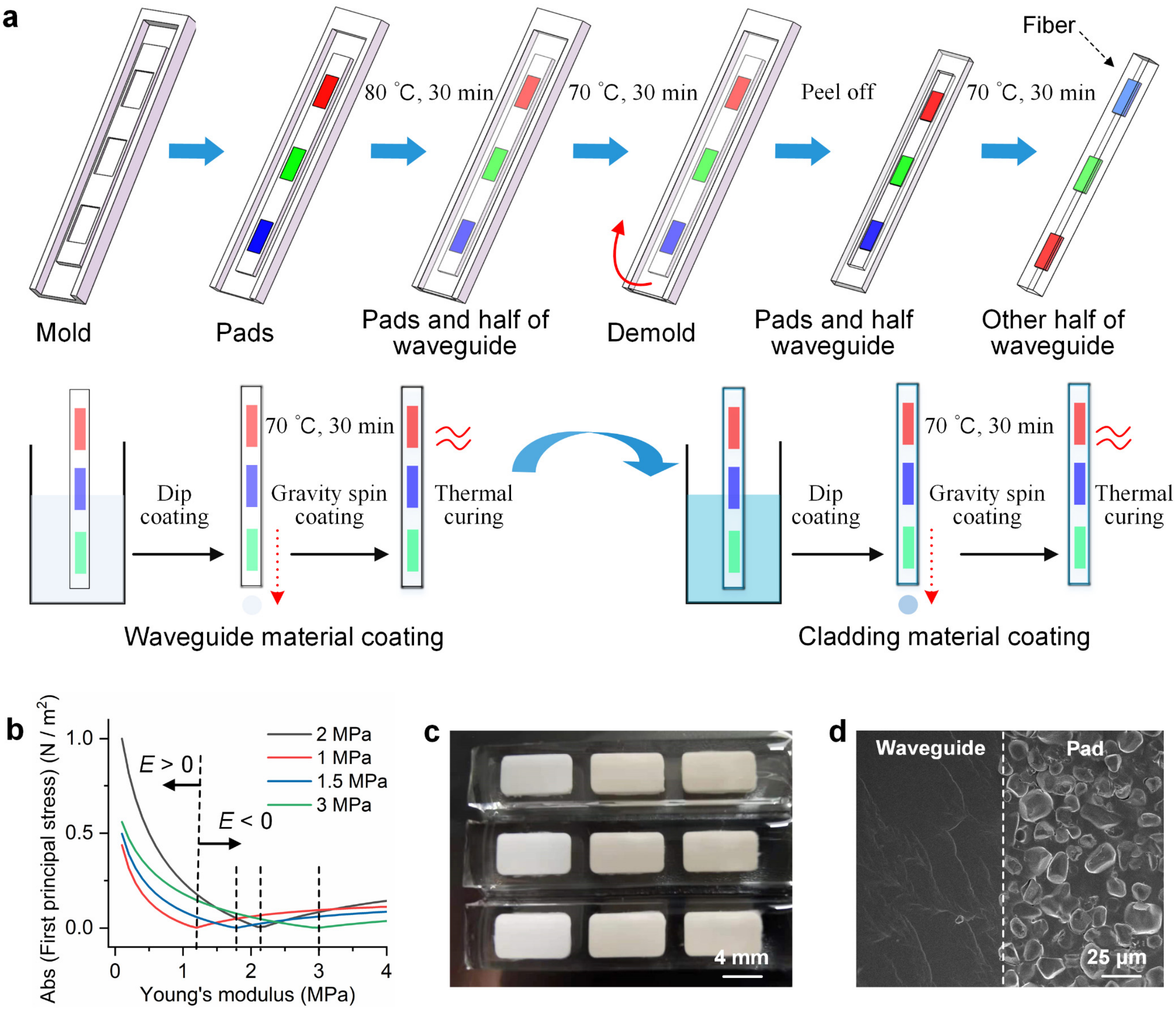

Extended Data Fig. 4 | Fabrication procedure and characterization of mechanoluminescence-powered distributed optical fibers (mp-DOFs). a, Flowchart for mp-DOF fabrication. The mechanoluminescent pad is made from ZnS:M phosphors and silica gel (monomer/curing agent, 10:1), with a mass ratio of 8:2. **b**, Young's modulus of waveguide materials versus mechanoluminescence. Relationship between the absolute value of the first principal stress ($|E|$) of the luminescent pad and M_{guide}, when M_{pad} is 1–3 MPa. "Abs" on the y-axis denotes the absolute value. M_{pad} and M_{guide} refer to the Young's modulus of the elastomeric materials used in the mechanoluminescent pad and waveguide, respectively. When $M_{guide} < M_{pad}$, i.e., within the range from the coordinate zero point to the inflection point of each curve in the figure, the first principal stress is positive. Thus, the luminescent pad mainly experiences tensile principal stress. In contrast, when $M_{guide} > M_{pad}$, the first principal stress is negative, and the pad experiences compressive principal stress. **c**, Optical image of the waveguide comprising mechanoluminescent pads. **d**, Scanning electron microscopy image of the waveguide and luminescent pad, showing well-dispersed ZnS:M@Al_2O_3 microparticles in silica gel.

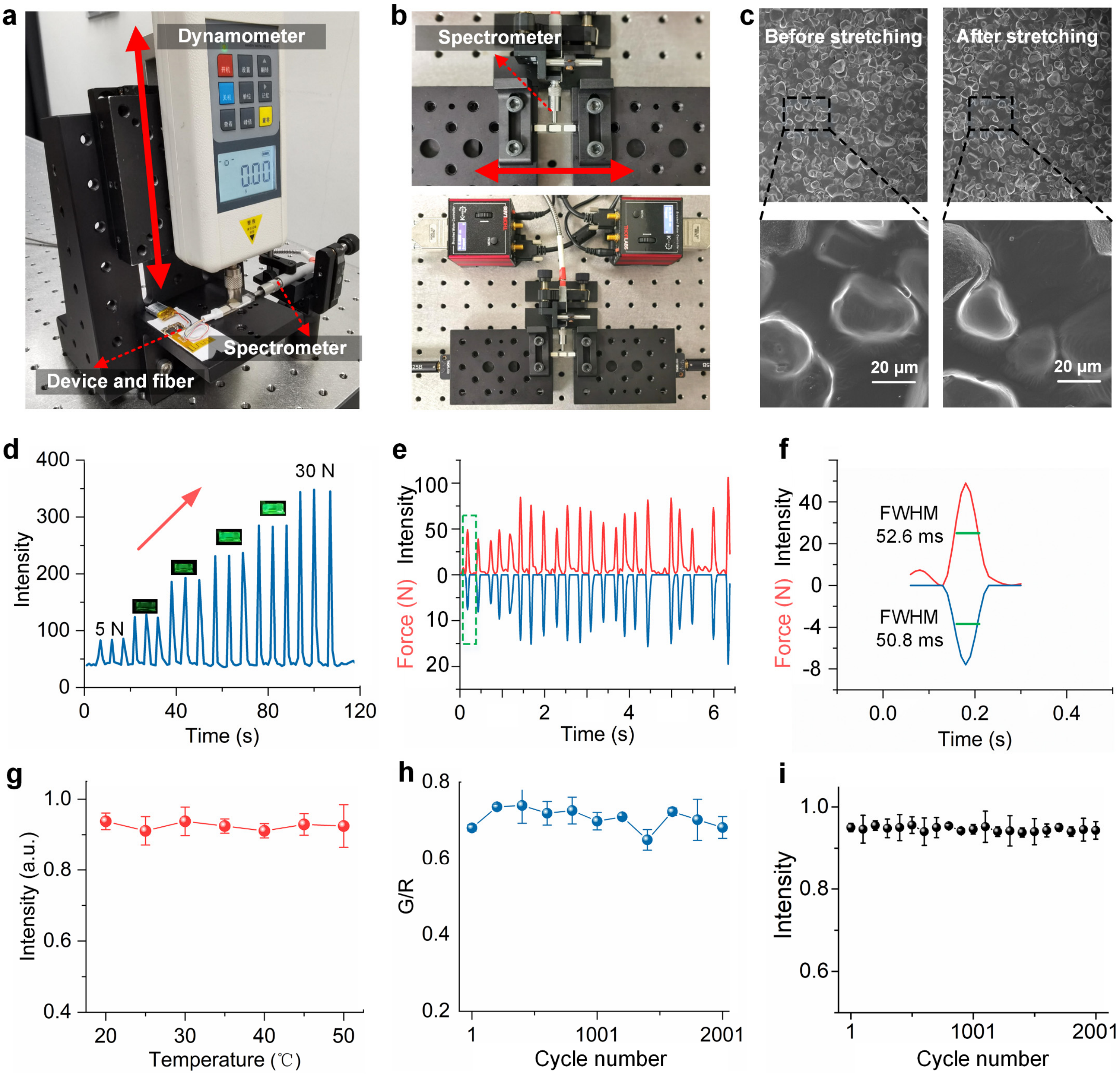

Extended Data Fig. 5 | Experimental setup and optical characterization of mp-DOFs. a, Force response test. A spectrometer (Ocean Optics QEPro) equipped with an optical fiber is used to record the spectral distribution and mechanoluminescence intensity. In addition, a force dynamometer (HP-100, Handpi Instruments Co, Ltd., China) is applied to record the force in real time. **b**, Cyclic extension test. During the experiment, two motorized stages stretch the fiber repeatedly, and the spectrometer records luminescence intensity. **c**, Scanning electron microscopy images of the luminescent pad before and after stretching over 2,000 cycles. **d**, Luminescence intensity versus applied force. **e**, Luminescence response to applied pulse force. **f**, Magnified luminescence response for one selected peak indicated by the dotted box in **e**. **g**, Luminescence intensity at different temperatures. **h**, Intensity ratio of green to red (G/R) emission, plotted over 2,000 cycles. **i**, Intensity of green emission, plotted over 2,000 compression cycles.

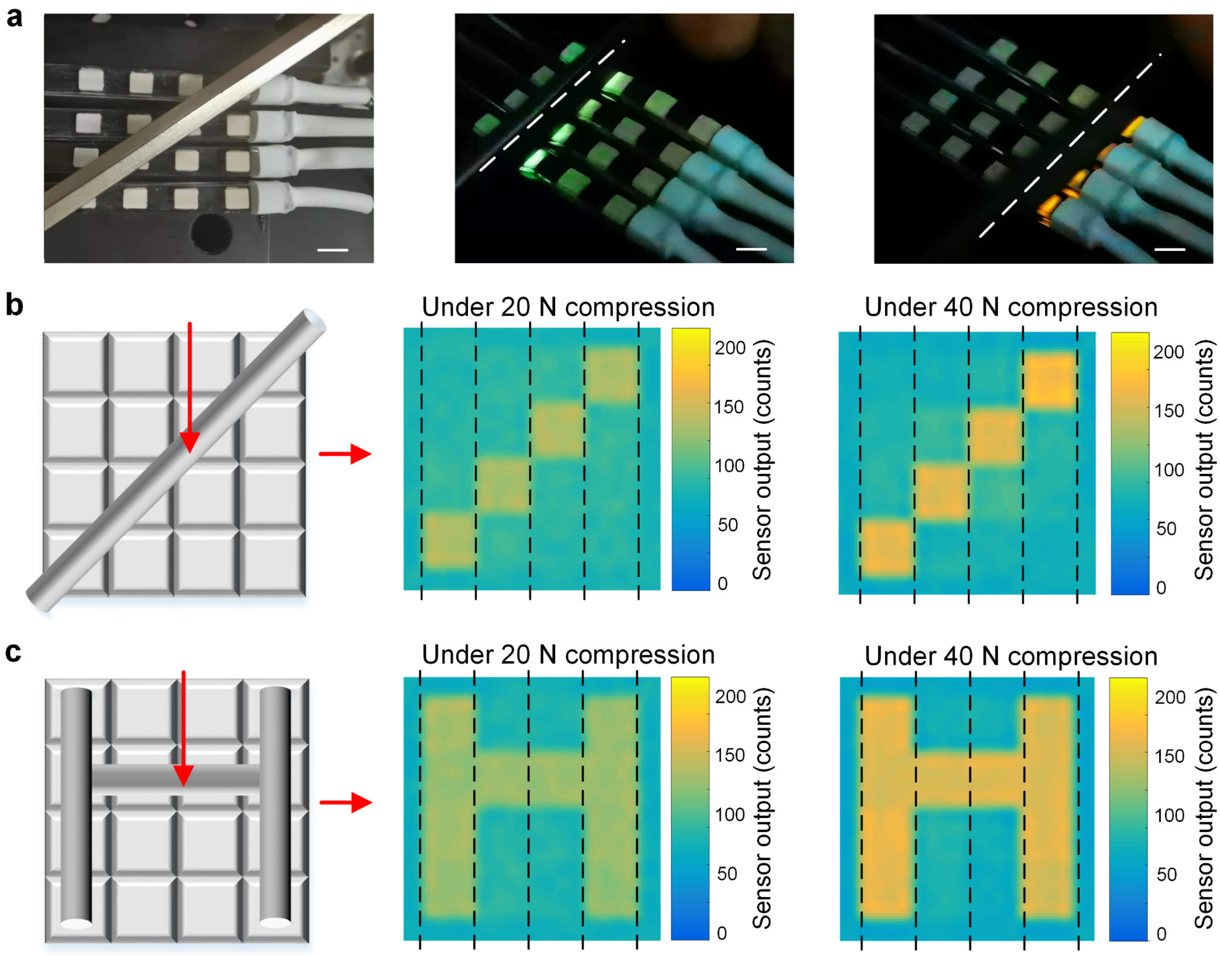

Extended Data Fig. 6 | Compression maps measured with a 4 × 4 mp-DOF array under different force patterns. Scale bars are 4 mm. **a**, Photographs of the 4 × 4 fiber array taken under various conditions (left to right: no pressing, pressing green-emitting pads, and pressing red-emitting pads). **b** and **c**, Recorded compression maps under different force levels through 1D and 2D force patterns, respectively.

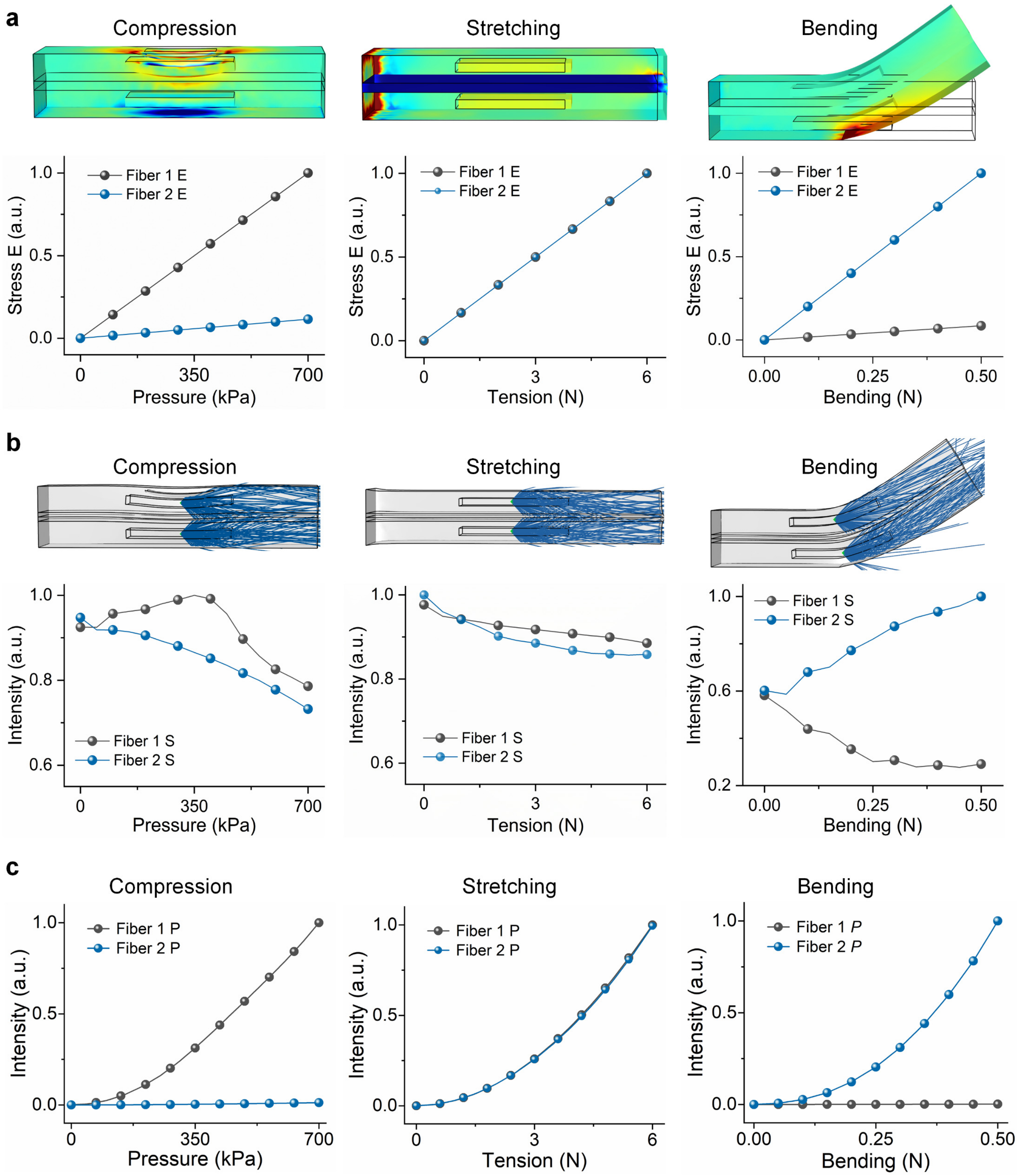

Extended Data Fig. 7 | Mechanical and optical properties of a double-layer mp-DOF under compression, stretching, and bending. **a**, The first-principal stress distribution mapping, and the average first-principal stress ***E*** versus the compressive, tensile, and bending forces. **b**, Ray tracing diagram and light intensity detected by the sensor ***S*** versus compressive, tensile and bending forces. **c**, Relationship between the detected intensity ***P*** at the fiber end and the amplitude of three stimuli obtained by substituting the results of ***E*** in **a** and ***S*** in **b** into formula $P = E^2S$.

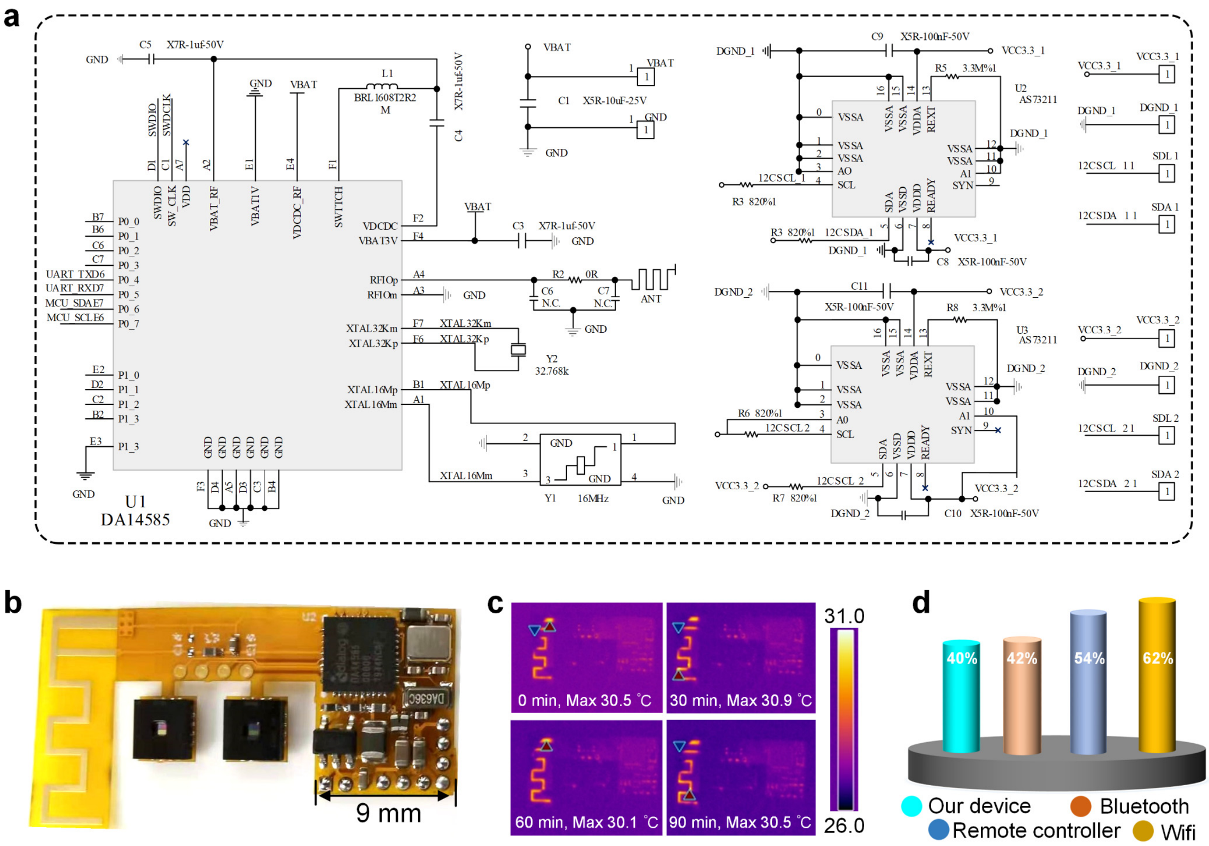

Extended Data Fig. 8 | Circuit schematic and characteristics. **a**, Circuit design for the interactive mouthguard. **b**, Image of the flexible printed circuit board. The 80-μm-thick circuit can be bent to fit the mouthguard. **c**, Thermal photos of the circuit board after varying periods of operation. **d**, Intensity of electromagnetic radiation from the circuit, equivalent to that of a mobile phone.

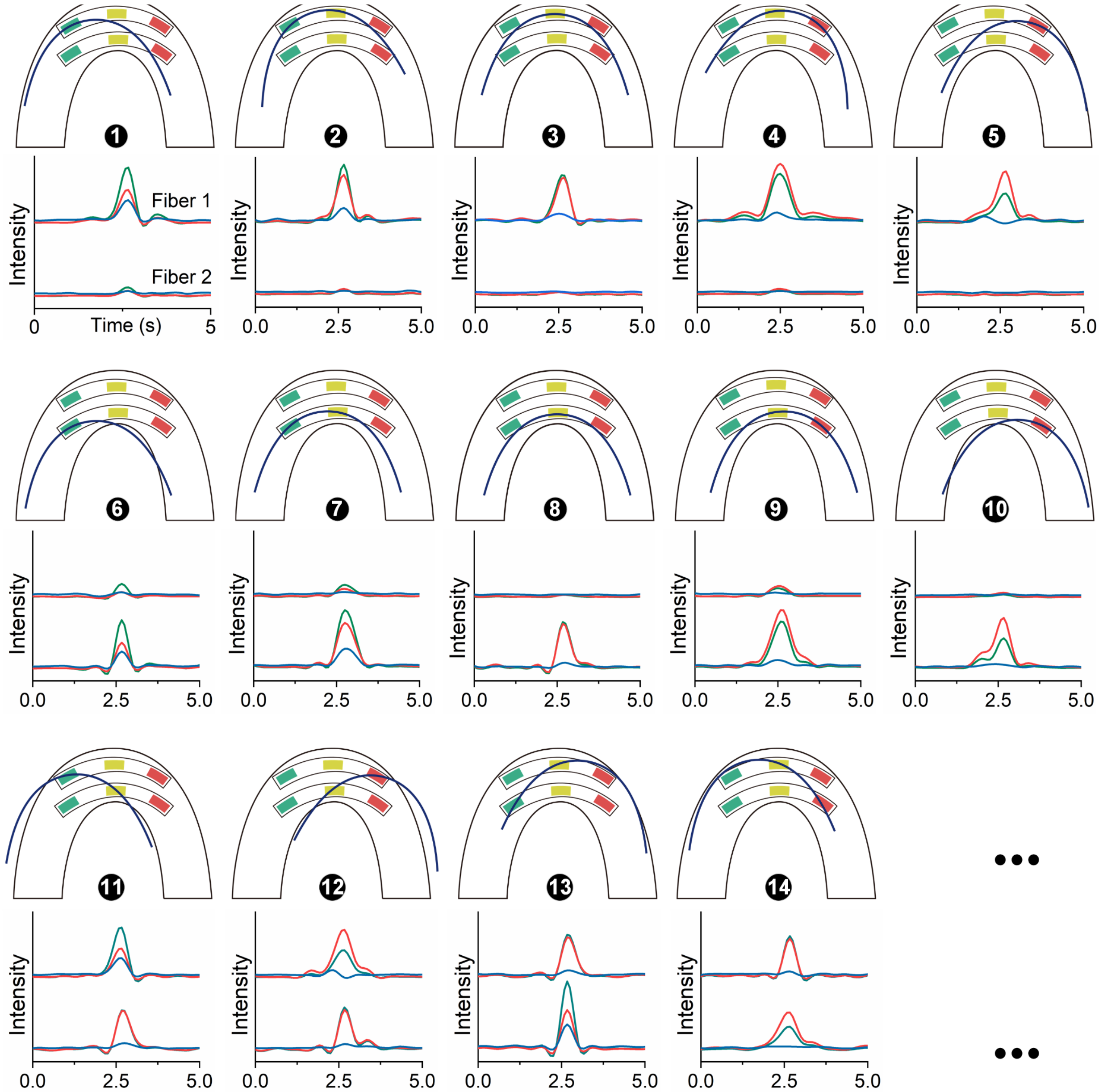

Extended Data Fig. 9 | Different occlusal patterns and corresponding tristimulus values. According to permutation and combination theory, there are 20 possible combinations using two mp-DOFs ($2C_5^1 + C_5^2 = 20$).

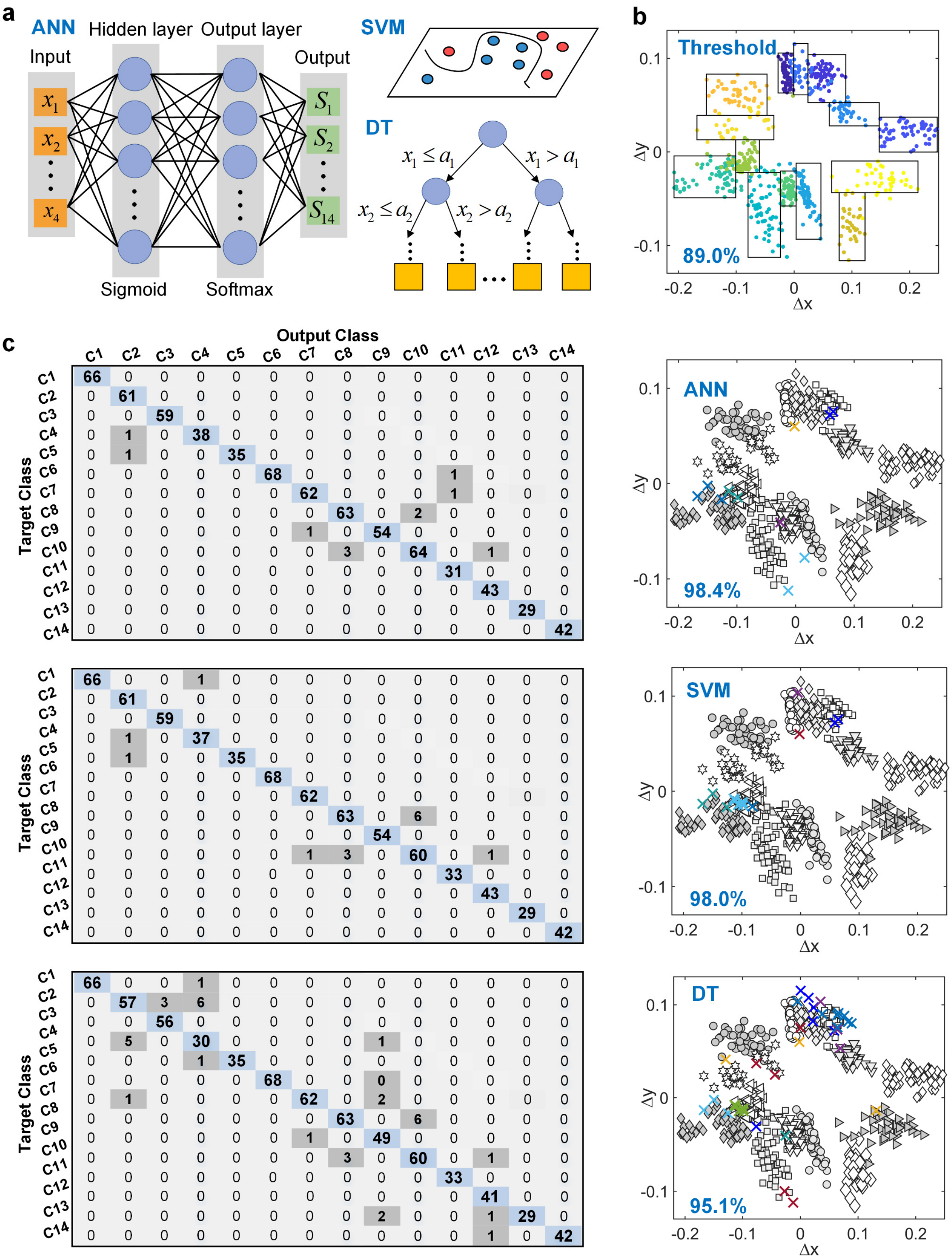

Extended Data Fig. 10 | Comparison of the results processed by the threshold evaluation, decision tree (DT), support vector machine (SVM), and artificial neural network (ANN). a, Schematic of DT, SVM, and ANN algorithms. **b**, Classification results processed using threshold evaluation, where the rectangles represent boundary lines. The classification accuracy is 89.0%. **c**, Classification results processed by the ANN, SVM and DT methods, including confusion matrices (left) and scatter plots (right). In the confusion matrix, the numbers in dark gray boxes indicate the number of misidentified data.

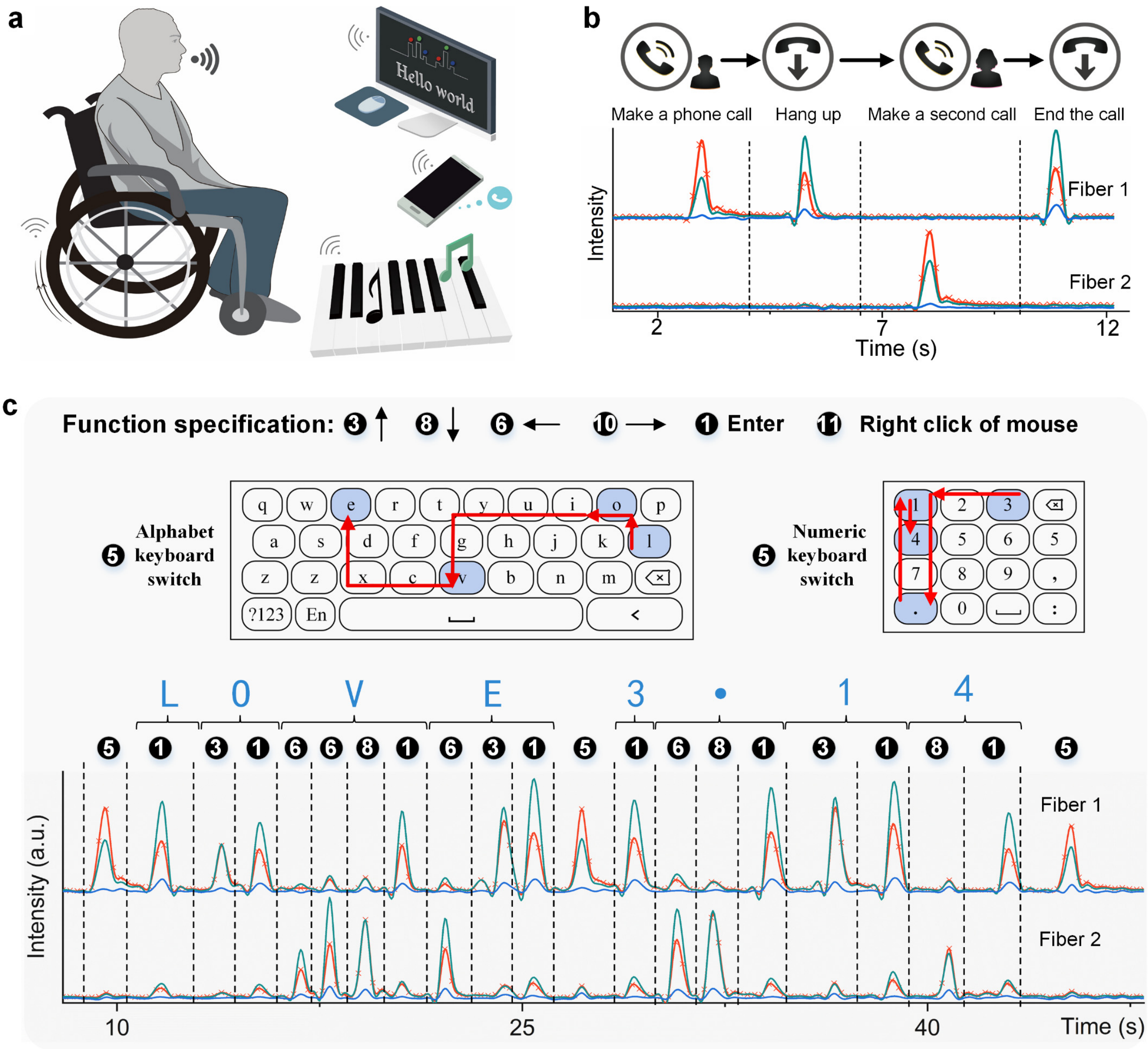

Extended Data Fig. 11 | Keyboard tying and phone call demonstration. a, The mp-DOF interactive mouthguard can assist people with disabilities in daily tasks. **b,** Real-time emission intensity signal recorded during phone operation using a custom smartphone app. **c,** (top panel) Correlation between functions and classification numbers shown in Extended Data Fig. 9. (middle panel) Navigation trajectory for typing letter keys “LOVE” and number keys “3.14.” Biting occlusal pattern 5 switches between numeric and alphabetic keyboards. (Bottom panel) Corresponding output signal of the color sensors. The red, green and blue curves represent tristimulus values *X*, *Y* and *Z*, respectively.

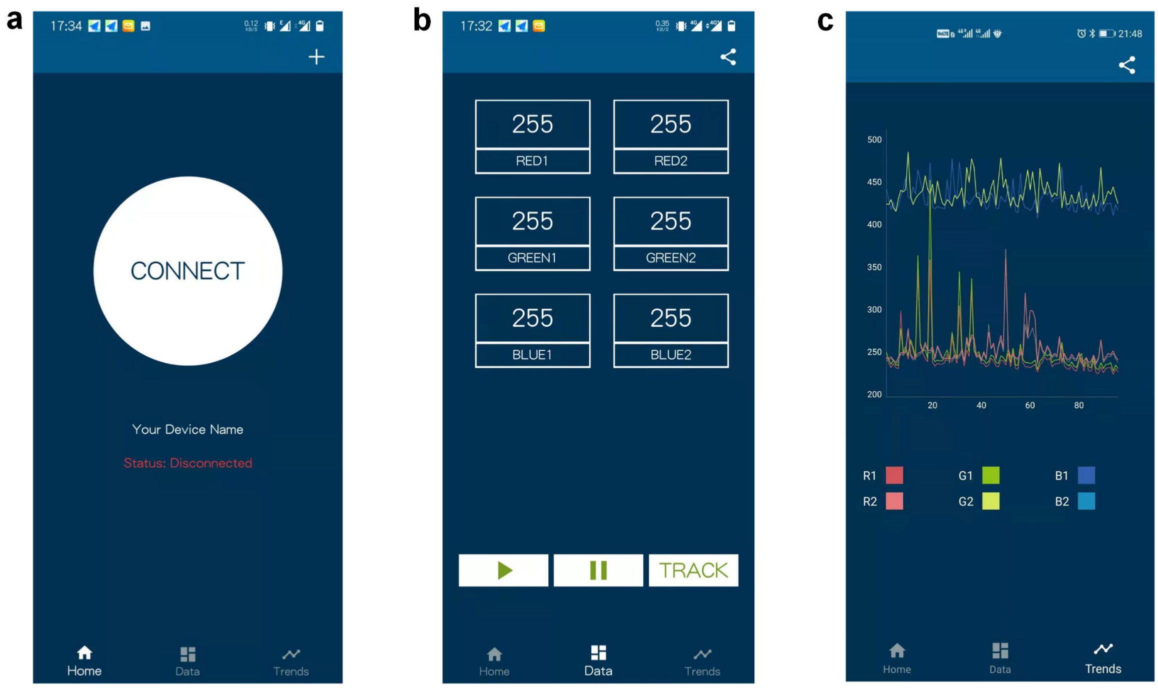

Extended Data Fig. 12 | Mobile application developed for data display and collection. a, Homepage of the application after Bluetooth pairing. **b**, Real-time display of data from the interactive mouthguard. **c**, Real-time data progression of an individual sensor.

Extended Data Fig. 13 | Demonstration of wheelchair navigation. a and **b**, Flexibility and accuracy test for wheelchair navigation over 1.6 km around a standard 400-m running track. Circular and figure-8-shaped wheelchair motion trajectories were recorded using the global positioning system (GPS) after five tests. Scale bar: 40 m.

Extended Data Table 1 | Characteristic comparison of reported sensors for mechanical stimuli.

Mechanism	Self-powered	Distributed detection[a]	Flexibility	Material	Deformation sensed	Power consumption	Reference
Piezoelectricity sensor	Yes	No	Yes	PDMS, polyester and stainless steel	Stretching	Zero	*Nat. Electron. 571, 578 (2020)*
Piezophotonic sensor	Yes	No	Yes	ZnS:Mn and PET	Compressing	Zero	*Nat. Photonics 7(9) (2013): 752. Adv. Mater., 2015, 27(14)*
Stretchable transistor	No	No	Yes	Carbon nanotubes and polymer	Stretching and compressing	Low	*Nature 555, 84 (2018)*
Piezoresistive sensor	No	No	Yes	Polybutylene and polyimide	Compressing	Low	*Nature 569, 699 (2019)*
Stretchable distributed fiber	No	Yes	Yes	Silica gel and dye	Compressing, bending and stretching	Large (>50 mW)	*Science 370, 848 (2020)*
Optical lace structure	No	No	Yes	Polyurethane	Compressing	Large	*Sci. Robot. 4, eaaw6304 (2019)*
Distributed acoustic sensor	No	Yes	No	Silicon	Stretching	Not reported	*Science 366, 1103 (2019).*
mp-DOF	**Yes**	**Yes**	**Yes**	**PDMS and doped ZnS**	**Compressing, bending and stretching**	**Zero**	**This work**

[a] Distributed detection here refers to a detection method that determines the changes in mechanical stimulus at different positions by detecting the optical signal at the fiber end.

Extended Data Table 2 | Elastomer materials in the literature and commercially available for stretchable fibers.

Ref	Structures	Materials	Elongation at Break	Tensile strength	100% Modulus	Refractive Index	Attenuation
(*1*)	Core	Polyurethane elastomer (Clear Flex 30)	675%	4.9 MPa	320 kPa	1.47	17%/3 mm
	Cladding	Silicone elastomer (Dragon Skin 20)	620%	3.8 MPa	260 kPa	1.41	90%–98%/3 mm
(*2*)	Core	Polyurethane rubber (VytaFlex 20)	1000%	1.4 MPa	340 kPa	1.461	2 dB/cm (860 nm)
	Cladding	ELASTOSIL M 4601 A/B	700%	6.5 MPa	500 kPa	1.389	1800 dB/cm (860 nm)
(*3*)	Core	Stretchable polyurethane fiber 'Stretch Magic'	NA	≈1 kg for 500 µm diameter	NA	1.52 (633 nm)	0.37 dB/cm (650 nm)
	Cladding	Silicone (ELASTOSIL M 4641 A/B)	>300%	4.5 MPa	NA	1.43 (633 nm)	
(*4*)	Core	Stretchable polyurethane fiber 'Stretch Magic'	NA	≈1 kg for the 500 µm diameter	NA	1.52	0.18 dB/cm
	Cladding	Air and EPU 40	300% (EPU 40)	9MPa (EPU 40)	3MPa (EPU 40)	n_{air} = 1 n_{EPU}=1.51 n_{porous}=1.24	
(*5*)	Core	Polystyrene-based polymer Star Clear 1044	693%	10.66 Mpa	0.75 MPa	1.52	1.2 dB/cm (400 nm) 0.8 dB/cm (855 nm)
	Cladding	Fluorinated polymer Daikin T-530	650%	10.8 MPa	1.9 MPa	1.36	
(*6*)	Core	PDMS (5:1)	134%	3.25 Mpa	1.28 MPa	1.424	1.2 dB/cm (500 nm) 0.9 dB/cm (675 nm) 0.5 dB/cm (850 nm)
	Cladding	PDMS (20:1)				1.417	
(*7*)	Core (no cladding)	Silicone LS-6941 (NuSil Technology)	95%	9 Mpa	None	1.41	0.05 dB/cm (visible)
(*8*)	Core	Silicone LS-6257 (NuSil Technology)	49%	0.84 Mpa	None	1.57	0.05 dB/cm (visible)
	Cladding	**PDMS (Sylgard®184)**	**140%**	**6.7 MPa**	**1.84 MPa**	**1.41**	**10%/2 mm**
(*9*)	Core	Room-temperature ionic liquid (RTIL), (1-ethyl-3-methylimidazolium ethyl sulfate, Alfa Aesar)				1.48	Low
	Cladding	SORTA–Clear 12	590%	2.2 MPa	158 KPa	1.41	NA
		LS-6143	125%	4.1 MPa	NA	1.43	3%/mm (visible)
		LS-6943	120%	6.2 Mpa	NA	1.43	0.05 dB/cm (visible)
		LS-6946	**275%**	**4.7 MPa**	**2.9 Mpa**	**1.46**	**<0.3 dB/cm (visible)**

References

1. Bai, H.D. et al. Stretchable distributed fiber-optic sensors. *Science* **370**, 848-852 (2020).
2. Zhao, H.C., O'Brien, K., Li, S. & Shepherd, R.F. Optoelectronically innervated soft prosthetic hand via stretchable optical waveguides. *Sci. Robot.* **1**, eaai7529 (2016).
3. Harnett, C. K., Zhao, H. C. & Shepherd, R. F. Stretchable optical fibers: threads for strain-sensitive textiles. *Adv. Mater. Technol.* **2**, 1700087 (2017).
4. Xu, P. A. *et al.* Optical lace for synthetic afferent neural networks. *Sci. Robot.* **4**, eaaw6304 (2019).
5. Leber, A., Cholst, B., Sandt, J., Vogel, N. & Kolle, M. Stretchable thermoplastic elastomer optical fibers for sensing of extreme deformations. *Adv. Funct. Mater.* **29**, 1802629 (2019).
6. Guo, J., Zhou, B., Yang, C., Dai, Q. & Kong, L. Stretchable and Temperature-Sensitive Polymer Optical Fibers for Wearable Health Monitoring. *Adv. Funct. Mater.* **29**, 1902898 (2019).
7. Martincek, I., Pudis, D. & Chalupova, M. Technology for the preparation of PDMS optical fibers and some fiber structures. *IEEE Photon. Technol. Lett.* **26**, 1446-1449 (2014).
8. Missinne, J. *et al.* Stretchable optical waveguides. *Opt. Express* **22**, 4168-4179 (2014).
9. Kim, T. *et al.* Heterogeneous sensing in a multifunctional soft sensor for human-robot interfaces. *Sci. Robot.* **5**, eabc6878 (2020).